



Fast Joule heating for transformation of Fe-MIL-125(Ti) to Fe/TiO₂ with enhanced photocatalytic activity in N₂ fixation

Huiying Yang^a, Guangmin Ren^a, Zizhen Li^a, Zisheng Zhang^b, Xiangchao Meng^{a,*}

^a Key Laboratory of Marine Chemistry Theory and Technology, Ministry of Education, College of Chemistry and Chemical Engineering, Ocean University of China, Qingdao 266100, China

^b Department of Chemical and Biological Engineering, Faculty of Engineering, University of Ottawa, Ottawa, Ontario K1N6N5, Canada

ARTICLE INFO

Keywords:

MIL-125(Ti)
Fe-doped titania
Joule heating
Nitrogen fixation
Active sites
Oxygen vacancy

ABSTRACT

It is critical to develop a highly efficient catalyst for the photocatalytic fixation of nitrogen to produce ammonia under ambient conditions. Herein, we reported on a fast Joule heating (FJH) method to synthesize 1.0 wt% Fe-doped TiO₂ (JH Fe/TiO₂) derived from MIL-125(Ti). For comparison, Fe/TiO₂ calcined in a tube furnace was also prepared (TF Fe/TiO₂). The photocatalytic production rate of ammonia on JH Fe/TiO₂ was increased to 56.87 μmol g⁻¹ h⁻¹, which was 1.5 times higher than that of TF Fe/TiO₂. As detected, FJH might lead to the formation of lattice defects with oxygen vacancies (OVs) formation. These OVs and defects had the potential to act as adsorption and reactive sites for N₂. Furthermore, in-situ infrared (FT-IR) along with Density Functional Theory (DFT) simulation were applied to study the possible reaction pathways of photocatalytic reduction of N₂. As calculated, the substitution of Fe³⁺ for Ti⁴⁺ with the formation of Fe-Ti dual active sites synergistically interacted with the OVs to facilitate the photocatalytic reduction process. Moreover, an alternative pathway was more favorable for the production of NH₃. The reasonable design of Fe-doped transition metal oxides and the proposed Fe-Ti dual active sites opened a new approach for highly efficient photocatalytic N₂ fixation.

1. Introduction

Ammonia is an essential feedstock for the production of artificial fertilizers, and also has recently been recognized as a promising hydrogen energy carrier [1–3]. Currently, ammonia is primarily produced via an energy-intensive Haber-Bosch process in industry. This process operates at high temperatures and pressures consuming fossil fuels and emitting large amounts of greenhouse gases [4–7]. Recently, photocatalysis has been realized to convert N₂ and H₂O to ammonia under ambient conditions. However, the photogenerated charge carriers' high recombination and sluggish reaction kinetics lead to low photocatalytic activity in the reduction of N₂ [8–10]. Therefore, it is essential to rationally design the photocatalysts to realize highly efficient conversion of N₂ to ammonia [11].

TiO₂, as the mostly studied photocatalyst, is characterized as non-toxicity, low cost, and high stability. TiO₂ derived from metal-organic frameworks (MOFs), such as MIL-125(Ti), has increasingly attracted attention. The derivative can maintain the porous structure of MOFs, producing open channels and abundant nano-size cavities, which are beneficial for highly-efficiently catalysis. For instance, Zhao *et al.* took

advantage of the porous nature of MIL-125(Ti) by calcining a mixture of MIL-125(Ti) and melamine to obtain N-TiO₂, which retained its internal porous properties. The photocatalytic performance of the optimal photocatalyst was improved in comparison to that of commercial TiO₂ [12]. Taking advantage of the MIL-125(Ti) large specific surface area, Chen *et al.* successfully prepared homogeneous flaky TiO₂/C nanocomposites with high specific surface area by calcining MIL-125(Ti), thus improving the photocatalytic efficiency of TiO₂/C [13]. However, the photocatalytic activity of TiO₂ formed by calcination with MOFs is still limited by the fast recombination of photogenerated carriers and the narrow wavelength range of photo-response. To further enhance the photocatalytic activity of TiO₂, the strategy of doping heteroatom is an easy and effective method [14,15]. The dopant was capable of trapping photogenerated charge carriers at the interface to inhibit the electron-holes recombination and activate the reactants by providing more reactive active sites on TiO₂ [16]. Fe is abundantly available and used in natural nitrogen fixation as a key component in biological nitrogen fixation enzymes [17,18]. Fe-based catalysts have also been widely used in the Haber-Bosch process to artificially produce ammonia. Fe doping has been reported as a promising approach to enhance the

* Corresponding author.

E-mail address: mengxiangchao@ouc.edu.cn (X. Meng).

<https://doi.org/10.1016/j.apcatb.2024.123795>

Received 10 November 2023; Received in revised form 8 January 2024; Accepted 30 January 2024

Available online 3 February 2024

0926-3373/© 2024 Elsevier B.V. All rights reserved.

photocatalytic reduction of N_2 to produce ammonia [17,19,20]. Typically, the heteroatom is usually doped into the support via a calcination process. Recently, our research group has reported on using a fast Joule heating (FJH) method to dope atoms into the support [21–24]. The FJH method occurs in a very short time (several seconds), which can avoid particle aggregation (generally a problem caused by the conventional calcination process) and fabricate lattice distortion and lattice defects. The FJH process is ideal for creating reactive sites, which might effectively improve the photocatalytic activity in N_2 fixation.

Herein, we reported on the conversion of MIL-125(Ti) to anatase TiO_2 along with Fe doping using the FJH method. As-prepared samples were systematically characterized by various techniques. With the formation of lattice defects and Fe doping, Fe- TiO_2 exhibited enhanced photocatalytic activity in the NRR. The mechanism of the great improvement was explored and discussed based on the experimental and theoretical simulation results. The possible reaction pathway and the reactive sites in photocatalytic reduction of N_2 to produce ammonia on Fe- TiO_2 have also been explored and discussed.

2. Experimental section

2.1. Chemicals

The chemicals, including methanol (MeOH, AR), N, N-Dimethylformamide (DMF, AR), Terephthalic Acid (PTA, AR), Titanium butoxide (TTIP, purity > 99.0%), and Iron (III) nitrate nonahydrate (Fe $(NO_3)_3 \cdot 9 H_2O$, 99.99% metals basis) were purchased from Macklin without other treatment. Nafion was supplied by Aladdin Ltd. (Shanghai, China).

2.2. Preparation of the MIL-125(Ti)

MIL-125(Ti) was prepared by a solvothermal method [25]. Typically, 3.53 g of PTA was dissolved in 6.0 mL of methanol and 54.0 mL of DMF under magnetic stirring. Then, 2.1 mL of TTIP as titanium precursor was added and magnetically stirred for 0.5 h. The well-dispersed solution was then sealed in a 100-mL stainless steel autoclave lined with PTFE and heated in an oven at 150 °C for 16 h. After natural cooling down to room temperature, the sample was separated, soaked in methanol for 12 h to remove the excess DMF, and then dried in a vacuum oven at 80 °C for approximately 12 h. As-prepared sample was labeled as MIL-125(Ti).

2.3. Preparation of the Fe/ TiO_2 composites

Different amounts (0.5 wt%, 1.0 wt%, 1.5 wt%, and 2.0 wt%) of Fe were added to MIL-125(Ti) by an impregnation method. Typically, MIL-125(Ti) (0.50 g) was dispersed in deionized water (40 mL) by magnetically stirring. Then, a designated amount of Fe $(NO_3)_3 \cdot 9 H_2O$ was added to the MIL-125(Ti) to form a slurry solution. The mixture was heated using a water bath at 60 °C for 6 h, and the solvent was evaporated at 80 °C in a vacuum oven for 12 h. Similarly, M-MIL-125(Ti) (where M = Co, Ni, Cu) was synthesized in a similar procedure using $CoCl_2$, $NiCl_2$, and $Cu(NO_3)_2$ (purchased from Macklin, 99.99% metals basis) as precursors. The sample of Fe-MIL-125(Ti) was further calcined by an FJH (Hefei in-situ technology Co., Ltd. China) under an Ar atmosphere. Four different temperatures (i.e., 500, 600, 700 and 800 °C) were selected for the experiment. Meanwhile, M-MIL-125(Ti) was calcined using the impregnation method to obtain JH M/ TiO_2 . The concentration of NO_3^- and Cl^- in JH M/ TiO_2 after calcination was found to be negligible (Figs. S1 and S2), the influence of which on the detection of ammonia could be ignored. Fe-MIL-125(Ti) was also calcined in a tube furnace (TF) under 600 °C for comparison.

2.4. Characterizations

X-ray diffraction (XRD) patterns obtained with the Miniflex600 using Cu $K\alpha$ radiation were used to characterize the phase composition and phase type of the prepared samples. Structural and morphological features were investigated by scanning electron microscopy (FE-SEM SU-8010) and transmission electron microscopy (TEM, Talos-F200X). Thermogravimetry (TGA, STA449F3) was used to study the weight loss of a sample as a function of temperature. The valence state and elemental composition of the prepared compounds were determined by X-ray photoelectron spectroscopy (XPS, Thermo Scientific ESCALAB Xi+) and in situ X-ray photoelectron spectroscopy (In situ XPS, Thermo Scientific ESCALAB 250Xi). A TU-1901 spectrophotometer (Pu xi Ltd. of Beijing, China) was used to record the UV-Vis diffuse reflectance spectra (DRS) of the samples. Transient lifetimes were recorded by Edinburgh-FLS1000 to study the recombination and migration of electron-hole pairs under 320 nm excitation. Electron paramagnetic resonance (EPR) was obtained with Bruker EMXPlus, which allowed the presence of electrons to be observed. The specific surface area was determined by the determination of N_2 adsorption-desorption isotherm by the Japanese Bayer BELCAT-B, and the specific surface area was determined by TPD testing. To reveal the photocatalytic mechanism of nitrogen fixation, in-situ infrared (FT-IR) spectroscopic measurements were performed using a synchrotron radiation source (Bruker INVENIO R FT-IR).

2.5. Electrochemical measurement

Electrochemical measurements were performed on an electrochemical workstation (CHI 660E, CH Instruments Inc). The standard three-electrode system consisted of a working electrode, a counter electrode (graphite carbon rod), and a reference electrode (saturated calomel electrode). Typically, the working electrode was prepared by dispersing 1 mg of photocatalyst and 5 μ L of Nafion solution in 40 μ L of deionized water, and then dropping 40 μ L of the solution onto an L-shaped glassy carbon electrode with a rubber-tipped dropper, and finally drying under an infrared lamp. The transient photocurrent and electrochemical impedance spectra (EIS) of the prepared samples were tested by using 0.5 M Na_2SO_4 aqueous solution as an electrolyte.

2.6. Photocatalytic N_2 fixation measurement

For the photocatalytic nitrogen fixation experiment, photocatalysts (30 mg) and distilled water (60 mL) were firstly added to a photoreactor. After fully sealing the reactor, N_2 (> 99.999% purity) was bubbled in the sealed reactor for 30 min. The reactor was then continuously irradiated with a 300 W Xe lamp (Beijing Perfect Lighting Co., Ltd.) for 1 h. The distance from the lamp to the vessel was calculated to be approximately 11 cm. After the reaction, 10 mL of the solution was filtered through a 0.22 μ m filter membrane to remove the residual catalyst powders. The filtered solution was then transferred to a 10-mL glass vial with addition of Nessler reagent. The Fe/ TiO_2 as the co-catalytic in the reactor promoted the change from N_2 to NH_4^+ , and the NH_4^+ concentration was quantified by spectrophotometry using Nessler's reagent and by ion chromatography (IC1826). In particular, excellent selectivity for N_2 photo-fixation was demonstrated with no N_2H_4 or NO_3^- detected as by-products. Meanwhile, the content of H_2O_2 after the reaction was tested. Then, apparent quantum efficiency (AQE) was further measured under filters of different wavelengths (365, 400, 500 and 600 nm). The photon flux of the incident light was measured with an optical power meter (CEL-NP2000–2(10)a, China). AQE was calculated according to Eq. 1 as follows :

$$AQE = \frac{N_e}{N_p} \times 100\% = \frac{3 \times N_{AM} \times N_A}{W \times A \times t \times h \times \nu} \times 100\% \quad (1)$$

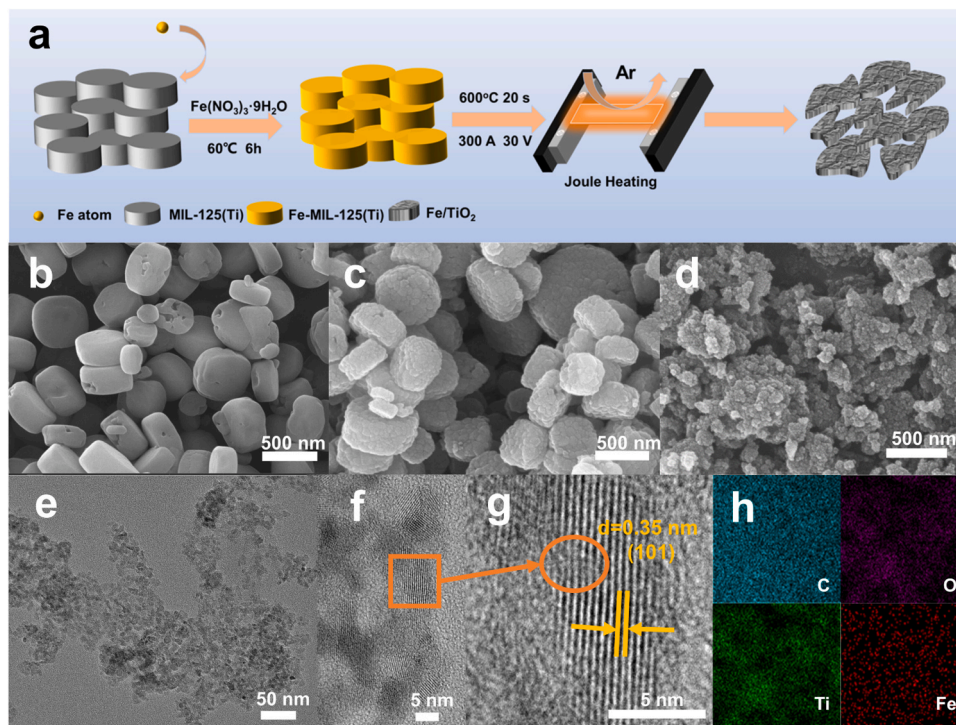


Fig. 1. (a) Schematic of JH Fe/TiO₂ preparation, SEM images of (b) MIL-125(Ti), (c) TF Fe/TiO₂ and (d) JH Fe/TiO₂, (e, f) TEM images of JH Fe/TiO₂ at different magnifications, (g) Enlarged TEM image, and (h) The corresponding C (blue), O (purple), Ti (green) and Fe (red) distributions of the EDX elemental mapping profiles.

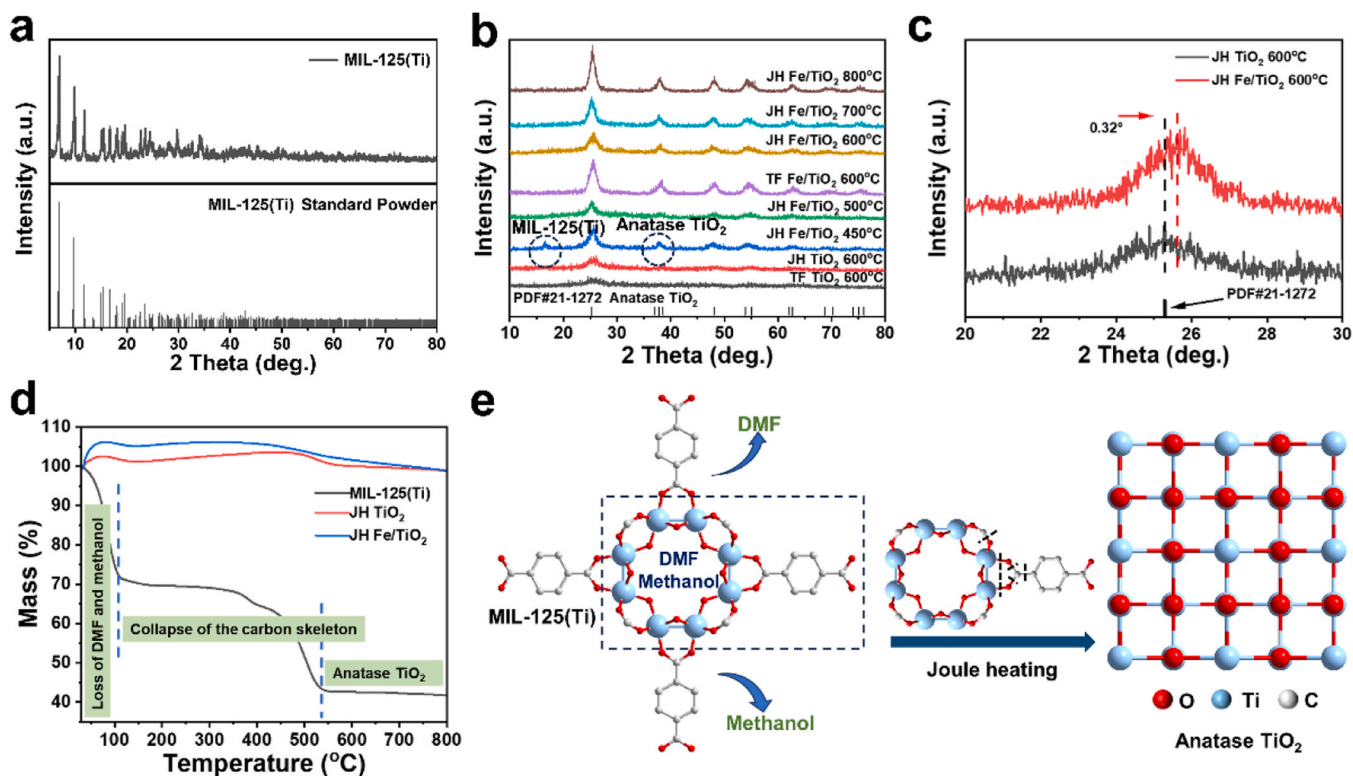


Fig. 2. XRD patterns of (a) MIL-125(Ti), (b) TiO₂ and Fe/TiO₂ with different preparation methods and different temperatures, (c) Enlarged XRD patterns, (d) TGA curves of MIL-125(Ti), JH TiO₂, JH Fe/TiO₂, and (e) Structural transformation from MIL-125(Ti) to anatase TiO₂.

where N_e and N_p are the total number of reactive electrons transferred and the number of incident photons, respectively. n_{AM} , W , A , t , and ν denote the number of moles of ammonia produced (mol), the intensity of

the incident light (measured as 491 mW cm^{-2}), the irradiation area (cm^2), the time (s) and the frequency, respectively. N_A and h are Avogadro's constant ($6.02 \times 10^{23} \text{ mol}^{-1}$) and Planck's constant ($6.62607015 \times 10^{-34} \text{ J}\cdot\text{s}$), respectively.

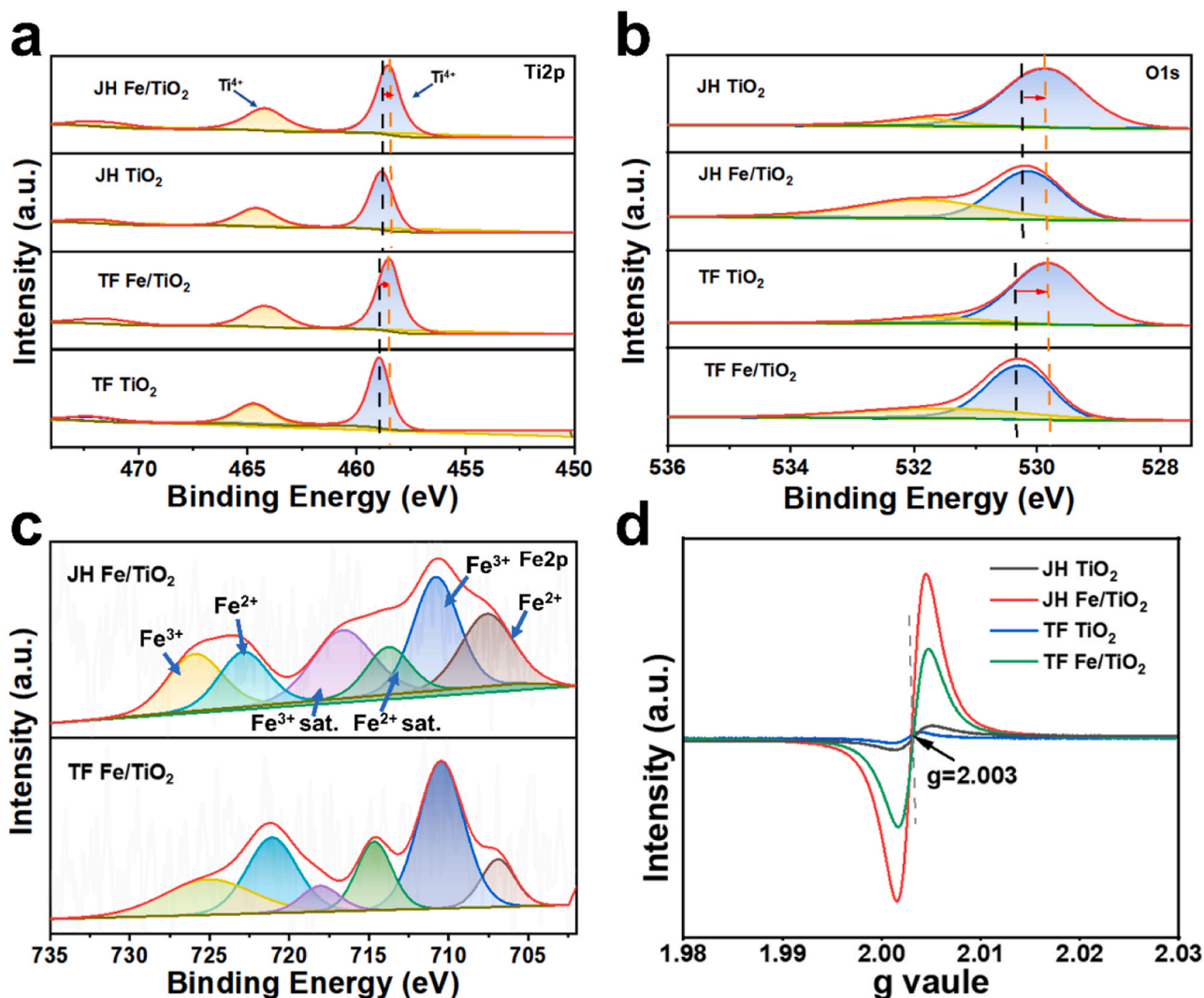


Fig. 3. XPS spectra of (a) Ti 2p, (b) O 1s, and (c) Fe 2p, and (d) EPR spectra for different samples.

3. Results and discussion

3.1. Preparation and characterization

As illustrated in Fig. 1a, Fe-MIL-125(Ti) has been synthesized using an impregnation method. Catalysts were treated at different temperatures (from 500 °C to 800 °C), modified with different metals (Cu, Fe, Co, and Ni) and different concentrations (0.5 wt%, 1.0 wt%, 1.5 wt%, and 2.0 wt%) by FJH treatment. The discussion would primarily focus on the characterization of Fe (1.0 wt%, 600 °C) doped MIL-125(Ti) in an argon atmosphere (Fe/TiO₂), which exhibited the highest ammonia production performance unless otherwise stated. SEM images showed that the MIL-125(Ti) was in the shape of cylinders, and the surface was relatively smooth (Fig. 1b). Fig. 1c exhibited that Fe/TiO₂ was obtained by calcination at 600 °C in a tube furnace (TF Fe/TiO₂), and its shape was slightly wrinkled compared to MIL-125(Ti). This unique pleated morphology provided the catalyst with a large specific surface area and abundant active sites, which was important for the catalytic performance. However, the original structure of Fe/TiO₂ prepared by the FJH method (JH Fe/TiO₂) was destroyed due to the high calcination temperatures, resulting in an irregular structure. TEM showed that small-sized TiO₂ was produced by the FJH method (Fig. 1e). Additionally, lattice defects were observed in JH Fe/TiO₂ due to the FJH calcination treatment, potentially providing more active sites (Figs. 1f and 1g).

Meanwhile, the lattice fringe of JH Fe/TiO₂ was measured as 0.35 nm, assigning to the (101) dominant facets of the anatase TiO₂ [26]. SEM and corresponding energy dispersive X-ray (EDX) elemental mapping images (Figs. 1g-1k) further confirmed the uniform distribution of Fe, Ti, and O elements in JH Fe/TiO₂. The successful doping of Fe into TiO₂ was also demonstrated.

XRD patterns of MIL-125(Ti), as depicted in Fig. 2a, agreed well with the standard patterns, indicating the successful preparation of MIL-125 (Ti) using the hydrothermal method [27]. Fig. 2b illustrated XRD patterns of Fe/TiO₂ prepared using the FJH method at various temperatures ranging from 450 °C to 800 °C. Clearly, TiO₂ and Fe/TiO₂ treated at the temperature from 500 °C to 800 °C showed characteristic diffraction peaks of anatase TiO₂ (PDF #: 21-1272). The peak at around 16° of JH Fe/TiO₂ treated at 450 °C belonged to incompletely conversion of MIL-125(Ti). This indicated that full conversion of MIL-125(Ti) could not be achieved at lower temperatures. Additionally, JH TiO₂ exhibited sharper peaks than TF TiO₂, suggesting that the FJH method accelerating the transformation of MIL-125(Ti) to anatase TiO₂. Compared with TiO₂ without doping, Fe-doped TiO₂ showed significantly narrower diffraction peaks, indicating a substantial increase in crystallinity after Fe doping [19,28]. Fig. 2c displayed the JH TiO₂ and JH Fe/TiO₂ enlarged XRD patterns at around 25°. It could be observed that the diffraction peaks of JH Fe/TiO₂ were gradually shifted towards a larger diffraction angle (0.32°) after Fe doping, indicating that Fe was

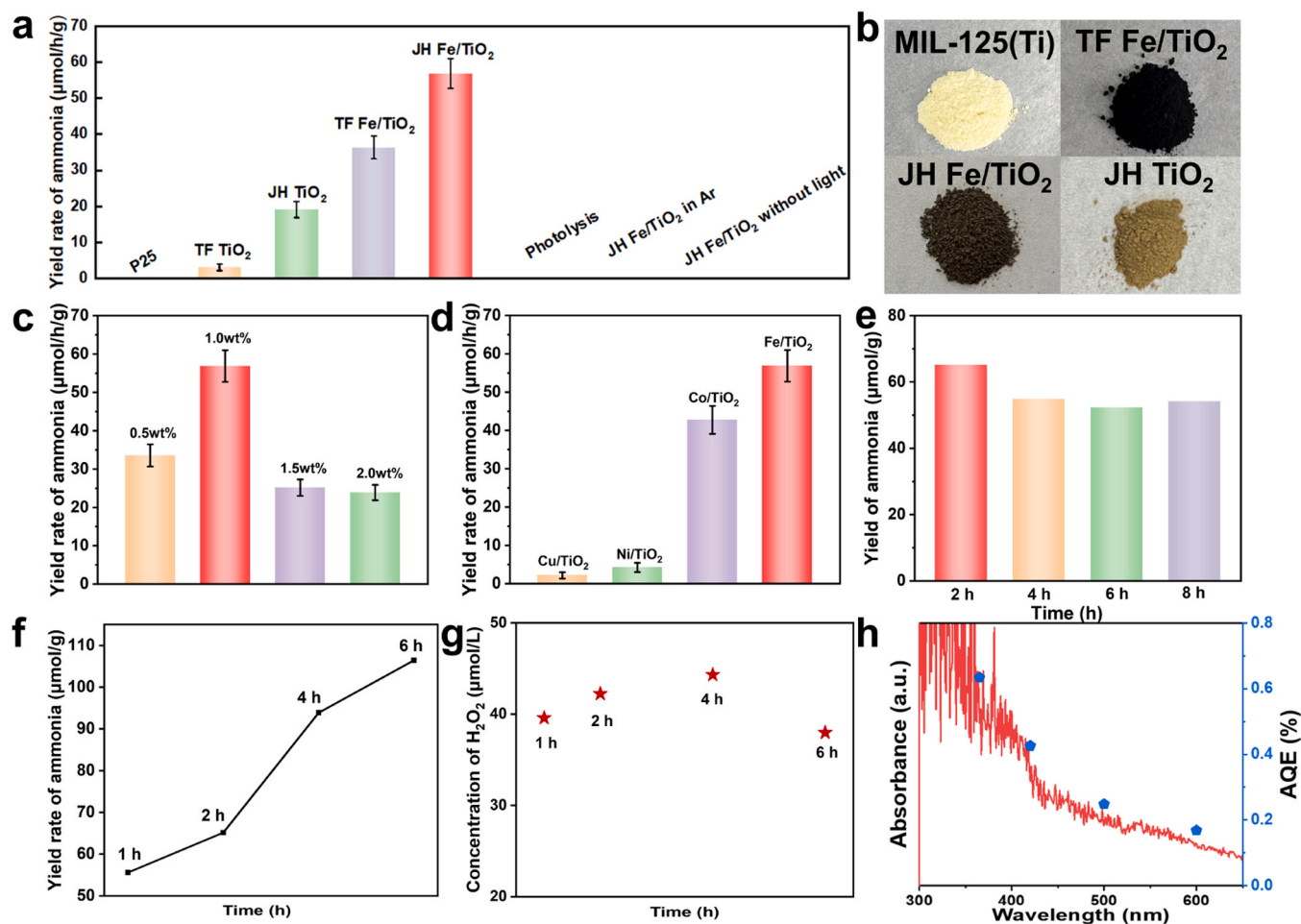


Fig. 4. (a) Photocatalytic nitrogen fixation activity of Fe/TiO₂ obtained from different conditions, (b) Photos of different samples, (c) Photocatalytic nitrogen fixation activity of JH Fe/TiO₂ with different Fe doping, (d) Photocatalytic nitrogen fixation activity of JH M/TiO₂ with different doped metals (M = Cu, Ni, Co, Fe), (e) Long cycle test of JH Fe/TiO₂, (f) Photocatalytic ammonia synthesis rate of JH Fe/TiO₂ (1.0 wt%, 600 °C) cyclic tests, (g) Concentration of H₂O₂ for photocatalysis on JH Fe/TiO₂, (h) AQEs (blue dots) and their photo-absorption spectra of JH Fe/TiO₂ (red line).

successfully doped into the crystal structure of TiO₂.

The thermogravimetric analysis (TGA) curve was primarily influenced by the porous structure of MIL-125(Ti) and its interaction with water (Fig. 2d). The weight loss curve could be divided into two segments occurring between 0 °C and 530 °C. The first segment involved a decrease in mass between 0 °C and 100 °C, which could be attributed to the removal of methanol, DMF (final residual methanol during MIL-125(Ti) synthesis), and small amounts of water from the pores. The second step resulted in a decrease in mass between 100 °C and 530 °C, possibly due to the pyrolysis of the metal-organic skeleton as a means of producing stabilized anatase TiO₂. This change from MIL-125(Ti) to anatase TiO₂ was demonstrated in Fig. 3e[29–31]. Negligible weight loss at the temperature between 530 °C and 800 °C was corresponded to the high stability of anatase phase when the treatment temperature higher than 500 °C as observed in the XRD analysis. The MIL-125(Ti) calcined with FJH as well as the Fe-doped MIL-125(Ti) showed better stability with minimal mass loss. The slight excess over 100% might be attributed to instrumental error [32].

The XPS survey spectrum of Fe/TiO₂ confirmed the presence of Fe, Ti and O elements[20]. As shown in Fig. 3a, compared to JH TiO₂ and TF TiO₂, the peak of JH Fe/TiO₂ and TF Fe/TiO₂ at 458.2 eV shifted towards smaller binding energies indicating successful Fe doping into TiO₂. For O 1 s peaks of TiO₂ and Fe/TiO₂, it could be seen that two peaks were deconvoluted (Fig. 3b). The peak at approximately 530.2 eV corresponded to the O²⁻ in TiO₂ lattice, while the higher binding energy at 532.1 eV belonged to the oxygen vacancy (OVs) [33]. The O1s XPS

results indicated that the variation rule of OVs was JH Fe/TiO₂ > TF Fe/TiO₂ > JH TiO₂. The OVs produced using the FJH method had a higher concentration compared to those produced using the tube furnace. This was due to the rapid heating and cooling process causing lattice distortions, resulting in the loss of lattice oxygen and the formation of OVs. Additionally, Fe doping promoted the formation of OVs, resulting in a decrease in the binding energy of Ti⁴⁺ and an increase in electron cloud density (Fig. 3a). The first hypothesis was that the binding energy of Ti-O decreased after the addition of Fe, leading to an increase in the concentration of oxygen vacancies. This inhomogeneous local charge distribution affected the local electron density of the adsorbed N₂, which helped to polarize the adsorbed N₂ for a better activation effect. Furthermore, Fe 2p peaks of JH Fe/TiO₂ and TF Fe/TiO₂ were shown in Fig. 3c. The Fe 2p spectra exhibited two characteristic peaks centered at 711.0 eV and 724.0 eV binding energies, attributed to Fe 2p_{3/2} and 2p_{1/2}, respectively. After deconvolution, the two peaks were resolved into two peaks at 708.9 eV and 723.5 eV, respectively, which were classified as Fe²⁺. The peaks at 711.7 eV and 725.8 eV corresponded to Fe³⁺. Meanwhile, the peak at 714.8 eV was identified as a satellite peak belonging to Fe 2p_{3/2} of Fe²⁺, while the peak at 717.6 eV was identified as a satellite peak belonging to Fe 2p_{1/2} of Fe³⁺ (Fig. 3c) [34,35]. To further demonstrate the role of FJH on oxygen vacancy formation, the EPR result (Fig. 3d) showed that OVs signaling was observed for all catalysts at a g value of 2.003. The concentrations of OVs in TiO₂ treated by the FJH method were both higher than that in TiO₂ treated by TF heating. The Fe-dopant accelerated the

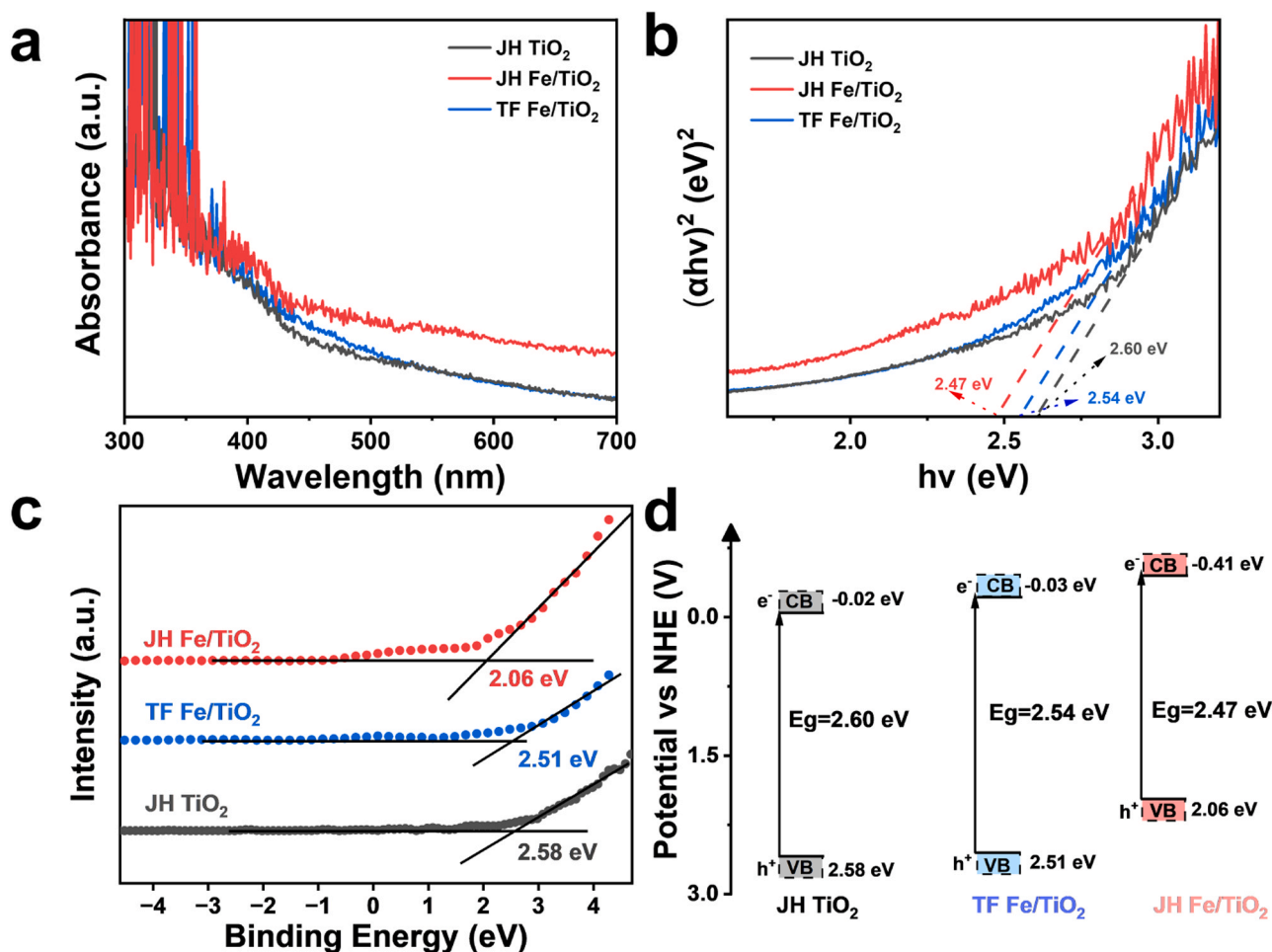


Fig. 5. (a) DRS spectra, (b) Tauc plots of $(\alpha h\nu)^{1/2}$ versus energy ($h\nu$), (c) XPS valence spectra, (d) Schematic diagrams of the band structure for different samples.

formation of OV, which might be due to the substitution of Fe³⁺ on the Ti⁴⁺ site, which left this site in an electron-rich state, forming an electronic defect. The increase of OV facilitated a higher efficiency of photocatalytic N₂ reduction.

3.2. Photocatalytic N₂ fixation tests

The photocatalytic activity in ammonia production was further tested. As illustrated in Fig. 4a, TF TiO₂ (3.17 $\mu\text{mol g}^{-1} \text{h}^{-1}$) as well as JH TiO₂ (19.21 $\mu\text{mol g}^{-1} \text{h}^{-1}$) showed higher ammonia-producing activity compared to commercial TiO₂ (P25), which indicated that TiO₂ (derived from MIL-125(Ti)) had better activity than P25. It might be due to OV in TiO₂ acted as reaction sites and promoted the activation of N₂. After adding Fe, the photocatalytic production rate of ammonia on JH Fe (1.0 wt%)/TiO₂ increased to 56.87 $\mu\text{mol g}^{-1} \text{h}^{-1}$, which was about 1.5 times higher than that on TF Fe/TiO₂. Notably, the activity in this work was higher than most of the reported photocatalysts (Table S1). Fig. 4b showed a comparison of the colors of the different catalysts, illustrating that calcination in an Ar atmosphere left a certain amount of carbon remaining resulting in a grey or black color. When the doping amount of Fe exceeded 1.0 wt%, the photocatalytic activity in ammonia production was decreased (Fig. 4c). The reduced photocatalytic activity might be due to the fact that excess Fe might block the reactive sites on TiO₂, and become recombination sites of photogenerated charge carrier. Other typical transition metals (such as Co, Ni, and Cu) were also doped into TiO₂ using the same procedure for comparison (Fig. 4d). The activity of Fe-doped TiO₂ was higher than other metals doped TiO₂. This might be due to Fe being selective to activate the N₂ and further improve the

photocatalytic activity in N₂ reduction, which has also been reported by others [19,36]. In addition, no significant photocatalyst inactivation was observed during the 8-h test (Fig. 4e), indicating that JH Fe/TiO₂ maintained good repeatability. Meanwhile, Fig. 4f showed that the ammonia concentration on JH Fe/TiO₂ increased linearly with the increase of reaction time, and the ammonia production reached 107.5 $\mu\text{mol g}^{-1} \text{h}^{-1}$ after 6 h of reaction. In addition, we explored the possible reaction pathways of photogenerated holes via detection of possible products. Fig. 4g demonstrated the concentration of produced H₂O₂. It indicated that the photogenerated holes might oxidize water to produce H₂O₂. A negligible amount of NO₃ was produced in the reaction, so the small amount of H₂O₂ that was produced did not oxidize the NH₃ to NO₃. To assess light utilization efficiency, we calculated the corresponding AQE by testing monochromatic light at various wavelengths (Fig. 4h). AQE was decreased as the wavelength of the monochromatic light increased (0.63% @365 nm, 0.45% @400 nm, 0.26% @500 nm and 0.18% @600 nm), which agreed well with photoresponsivity as detected in the DRS test of JH Fe/TiO₂.

3.3. Optical and electronic properties

UV-Vis DRS was utilized to investigate the optical properties of the prepared samples [37]. As shown in Fig. 5a, TiO₂ only absorbed light in the UV region (200 nm - 400 nm). With the introduction of Fe, TF Fe/TiO₂ as well as JH Fe/TiO₂ showed a small amount of absorption in the visible region (400 nm - 700 nm). It could be assumed that the introduction of Fe and the formation of OV broadened the spectrum of light absorption. According to the Tauc plots (Fig. 5b), the band gaps of

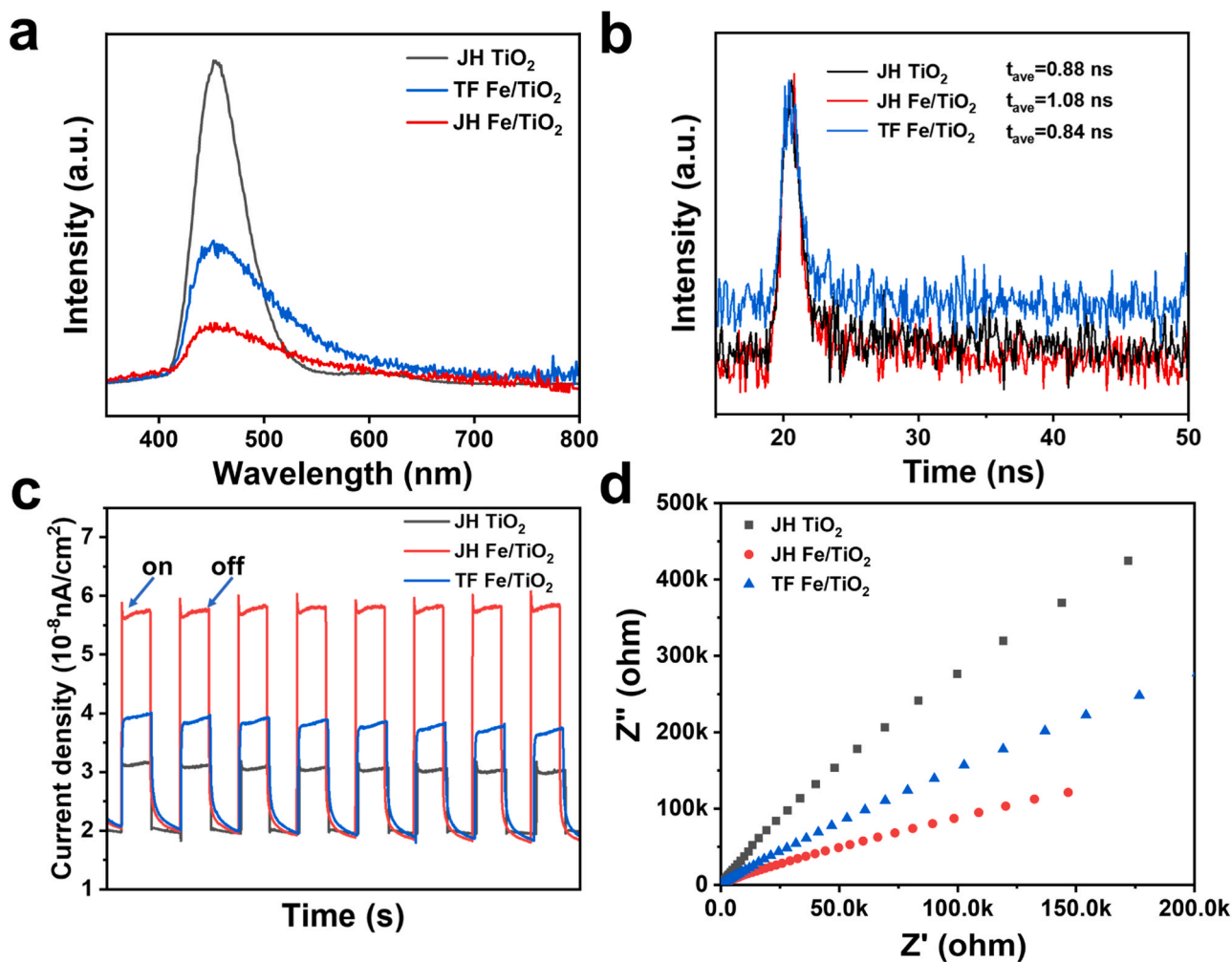


Fig. 6. (a) PL spectra, (b) Time-resolved transient PL decay, (c) Photocurrent responses, and (d) EIS for prepared samples.

JH TiO₂, TF Fe/TiO₂, and JH Fe/TiO₂ were calculated as 2.60 eV, 2.54 eV, and 2.47 eV, respectively. Doping Fe into the lattice of TiO₂ has been proven to narrow the band gap. In addition, the XPS valence band (VB) spectrum indicated that the VB energy levels of JH TiO₂, TF Fe/TiO₂, and JH Fe/TiO₂ were 2.58 eV, 2.52 eV, and 2.06 eV, respectively (Fig. 5c). Based on the band position equation ($E_g = E_{VB} - E_{CB}$) [37], the conduction bands (CB) corresponding to JH TiO₂, TF Fe/TiO₂, and JH Fe/TiO₂ were calculated as -0.02 eV, -0.03 eV, and -0.41 eV, respectively (Fig. 5d). The slightly higher CB after Fe doping was more thermodynamically conducive to the photoreduction reaction of nitrogen, and therefore JH Fe/TiO₂ exhibited the best ammonia production activity.

As shown in Fig. 6a, the PL intensity of JH Fe/TiO₂ was lower than JH TiO₂ and TF Fe/TiO₂, indicating that the synergistic interaction of Fe with OV could accelerate charge transfer and inhibit electron-hole recombination. Meanwhile, the average fluorescence lifetime of JH TiO₂, TF Fe/TiO₂, and JH Fe/TiO₂ was calculated as 0.88 ns, 0.84 ns, and 1.08 ns, respectively (Fig. 6b). This difference in lifetime might be due to the presence of OV, which could form surface defects and trap electrified state electrons. This hindered the direct recombination of electron-hole pairs produced by light, thus prolonging the lifespan of photogenerated electrons [22]. Fig. 6c exhibited that the photocurrent responsivity of JH Fe/TiO₂ was much higher than either TF Fe/TiO₂ or JH TiO₂. In EIS spectroscopy (Fig. 6d), the circular radius of JH Fe/TiO₂ was much smaller than JH TiO₂ and TF Fe/TiO₂, indicating that JH Fe/TiO₂ had higher charge transfer and separation efficiency [38].

3.4. Exploration of Active Sites

The N₂ adsorption behavior of the catalysts was investigated by N₂-TPD measurements. As could be seen from Fig. 7a, the N₂ desorption signal peak of TF TiO₂ was weak. The peaks between 100–200 °C might be due to the physical adsorption of N₂ on JH Fe/TiO₂. In addition, new desorption peaks of JH Fe/TiO₂ and TF TiO₂ were observed at 370 °C, suggesting that the OV influenced the adsorption of N₂ to a certain extent. The desorption peak of JH TiO₂ was observed at 520 °C, while the position of the peak position of JH Fe/TiO₂ located at 520 °C shifted to a higher temperature. Meanwhile, the total amount of N₂ desorbed on the JH Fe/TiO₂ sample was higher than JH TiO₂ based on the TPD peak area. These observations suggested that Fe doping created novel active sites for N₂ adsorption.

To elucidate the potential mechanism between Fe and TiO₂, in situ XPS experiments were employed as the foundation for detecting electron transfer generated by the catalysts [39]. As shown in Fig. 7b, Ti 2p_{3/2} was observed at 458.2 eV and the Ti 2p_{1/2} was observed at 464.7 eV of JH Fe/TiO₂, which were assigned to Ti⁴⁺. After illumination, new peaks appeared at 458.2 eV and 461.8 eV, which were assigned to Ti³⁺. This study demonstrated that the presence of Ti³⁺ prompted the creation of OV between the valence and conduction bands, leading to an improvement in both visible light absorption and photocatalytic activity [40,41]. For the Fe 2p spectrum after deconvolution (Fig. 7c), the peaks at 708.9 eV and 723.5 eV were decomposed into two peaks assigned to Fe²⁺, while the peaks at 711.7 eV and 725.8 eV correspond to Fe³⁺. Meanwhile, the peak at 714.8 eV was identified as the satellite peak

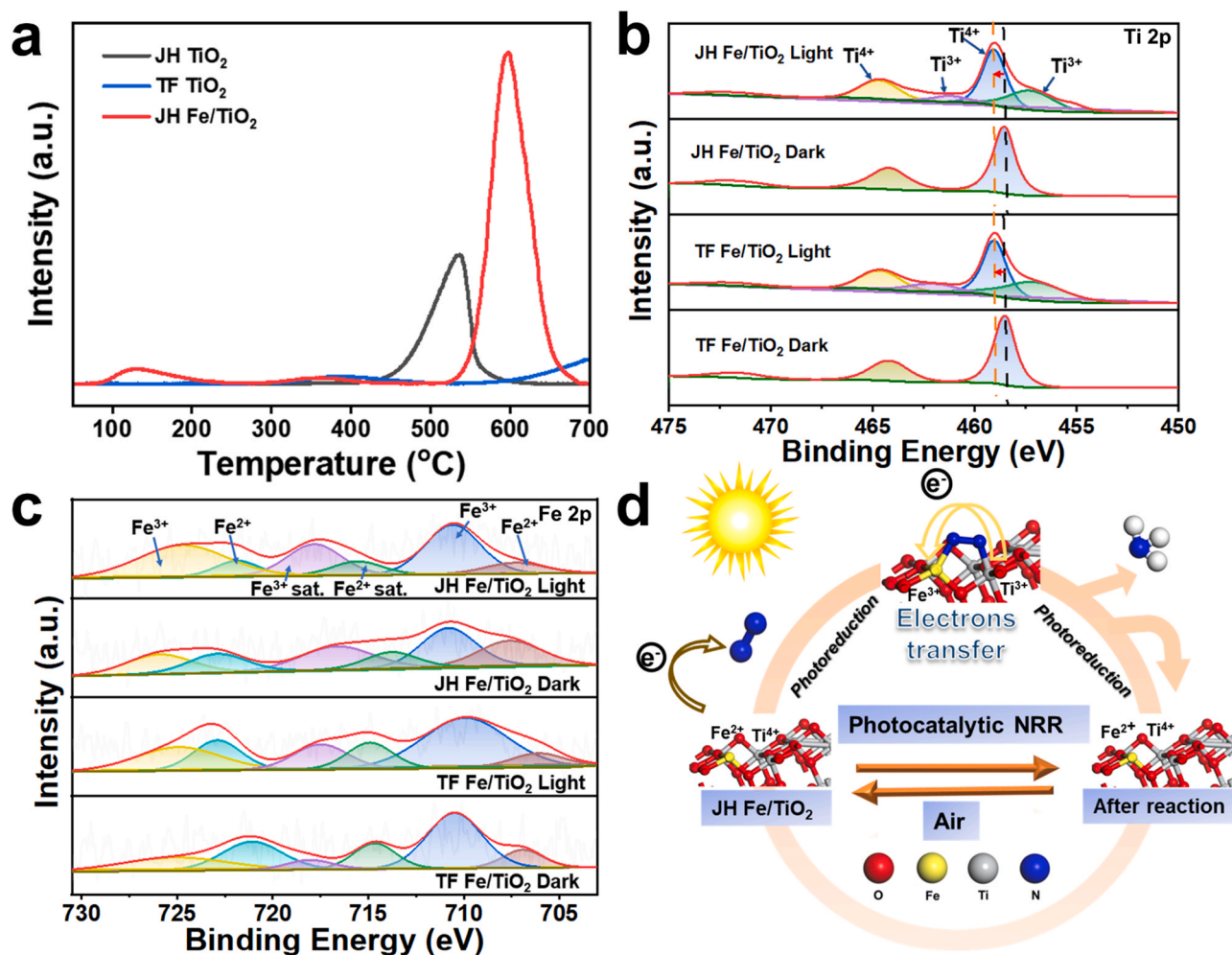


Fig. 7. (a) N₂-TPD spectra of different samples, in-situ XPS for (b) Ti 2p, (c) Fe 2p of JH Fe/TiO₂, TF Fe/TiO₂, and (d) Schematic representation of the charge transfer over Fe/TiO₂ in photocatalytic NRR process.

belonging to Fe 2p_{3/2} Fe²⁺ and the peak at 717.6 eV belonged to Fe 2p_{1/2} Fe³⁺ [20]. Upon switching on the lamp, two new peaks of Ti³⁺ emerged, indicating that some of the Ti⁴⁺ gained electrons and changed to Ti³⁺. Meanwhile, the Fe³⁺/Fe²⁺ peak area ratio for TF Fe/TiO₂ ranged from 1.38:1 to 2.22:1, and for JH Fe/TiO₂ it ranged from 1.47:1 to 3.50:1. Thus, the peak area of Fe²⁺ decreased and the peak area of Fe³⁺ increased, indicating that some of Fe²⁺ lost electrons and changed to Fe³⁺. Based on the previous section, Fig. 7d displayed the changes in charge transfer and valence of Fe and Ti following N₂ adsorption by JH Fe/TiO₂. Electrons were transferred from Fe to Ti, forming Fe-Ti dual active sites to achieve efficient adsorption and activation of N₂[42]. After turning off the light, Fe sites gradually recovered to their initial chemical states, forming a cycle of Fe²⁺ → Fe³⁺ → Fe²⁺. Therefore, the Fe-Ti dual active sites could effectively translocate and utilize photo-generated carriers to promote N₂ activation.

To reveal the photocatalytic mechanism of nitrogen fixation by JH Fe/TiO₂ catalysts, in situ infrared spectroscopic measurements were performed using a synchrotron radiation source[43]. Fig. S3 showed the FT-IR during photocatalytic nitrogen fixation for up to 60 min. Several vibrational bands could be identified, namely, peak at 3555 cm⁻¹ due to N-H stretching, peak at 3360 cm⁻¹ due to adsorbed -OH, peak at 1624 cm⁻¹ due to adsorbed N₂, peak at 1557 cm⁻¹ due to adsorbed NH₃, peak at 1360 cm⁻¹ due to adsorbed NH₄⁺ species, and peak at 1060 cm⁻¹ due to NH₂-NH₂ stretching. It should be noted that the characteristic peaks belonging to N-H and NH₂-NH₂ groups at 3555 and 1060 cm⁻¹ were the transition states from N₂ to NH₄⁺ in the nitrogen fixation

reaction[44,45]. Taken together, these results revealed the reaction pathways of N₂ transfer and also indicated that the rapid adsorption of nitrogen on JH Fe/TiO₂ might be responsible for its excellent nitrogen fixation performance. An experimental basis was provided for the following DFT simulation of the reaction pathway exploration.

3.5. Photocatalytic nitrogen fixation reaction mechanism

The possible reactive sites and electron transfer were further determined through DFT calculation. Firstly, the locations of OV in pristine TiO₂ were explored, and then, the adsorption of N₂ on a modified TiO₂ (101) surface with OV was calculated. As shown in Fig. 8a, the adsorption energy of N₂ on five-coordinated Ti (Ti₅), six-coordinated Ti (Ti₆), five and six-coordinated Ti (Ti₅-Ti₆) were 0.36 eV, 0.43 eV, 0.33 eV, respectively. And due to the adsorption energy being lower on Ti₅-Ti₆, it preferred the Ti₅-Ti₆ atomic sites. Meanwhile, N≡N bond adsorbed on Ti₅-Ti₆, the bond length of N≡N extended to 1.176 Å, indicating greater strength than the adsorption on Ti₅ (1.132 Å) and Ti₆ (1.110 Å). It suggested that the N₂ underwent a strong polarization, which verified that Ti₅-Ti₆ was a favorable coordination conformation. Besides, the bond length of original N≡N was 1.100 Å [46], while the bond lengths on TiO₂-OV were all higher than this value, which indicated that the OV promoted nitrogen activation. Furthermore, adsorption energies were calculated after doping Fe on pristine TiO₂. It could be observed that the adsorption energy of N₂ adsorbed on Fe/Ti bridge site was 0.11 eV and the value was lower than N₂ on Ti (0.18 eV)

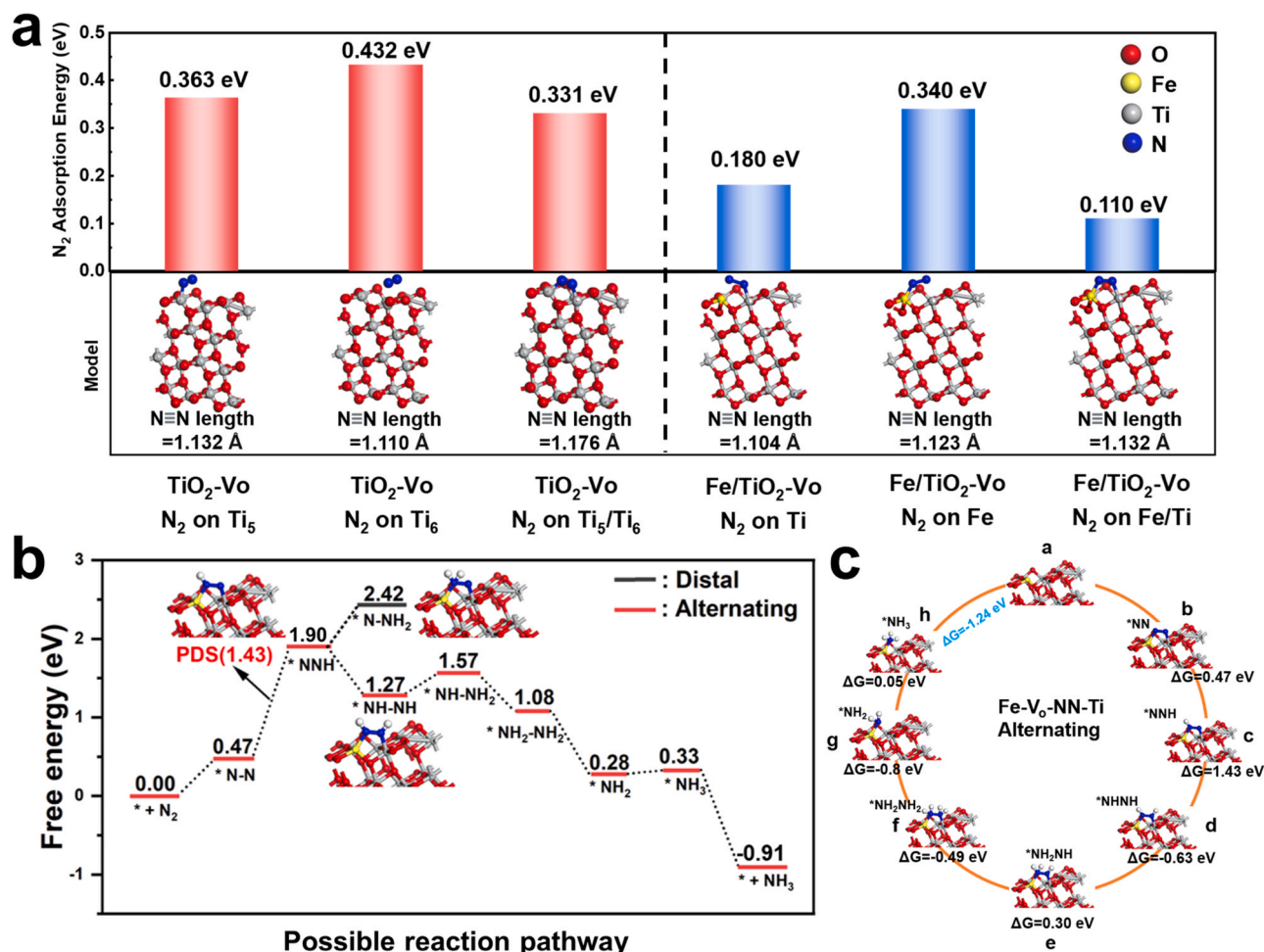


Fig. 8. (a) The structure of N₂ adsorbed onto distinct sites of the catalyst and their adsorption energies, (b, c) Free energy diagrams of the distal and alternative mechanisms for the N₂ reduction on JH Fe/TiO₂.

and on Fe (0.32 eV). The results thus indicated that N₂ preferred Fe/Ti bridge-site adsorption, which agreed with the in situ XPS analysis and the bond length of N≡N was measured below for further verification. The bond length of N≡N adsorbed at the Fe/Ti bridge site was 1.132 Å higher than that adsorbed on Fe (1.123 Å) and the bond length adsorbed on Ti (1.104 Å). Thus, it proved that the Fe/Ti bridge adsorption was the optimal conformation. Experimental and theoretical calculations showed that the Fe/Ti dual active site with OV played an effective synergistic role while adsorbing, activating N₂, and promoting electron transfer to N₂.

Since N₂ adsorption occurred in a bridged manner, the Gibbs free energy (ΔG) of hydrogenation in the distal and alternative pathways of the dual active site was modeled. As could be seen from Fig. 8b, there were two processes for the hydrogenation of *NNH, producing *NNH₂ (distal pathway) and *NHNH (alternative pathway). The ΔG of the distal pathway (0.52 eV) was higher than that of the alternative pathway (-0.63 eV). Therefore, N₂ typically underwent hydrogenation through an alternative pathway (*N₂ → *NNH → *NHNH → *NHNH₂ → *NH₂NH₂ → *NH₂NH₃ → *NH₃) to be hydrogenated [37,47]. Fig. 8c presented the modeling of the alternating pathway and the adsorption energy changes, with the breaking of the N≡N bond ($\Delta G = 0.47$ eV), the ΔG for the first hydrogenation of N₂ to *NNH was 1.43 eV. And the subsequent processes occurring as *NNH → *NHNH ($\Delta G = -0.63$ eV), *NHNH → *NHNH₂ ($\Delta G = 0.30$ eV), *NHNH₂ → *NH₂NH₂ ($\Delta G = -0.49$ eV), *NH₂NH₂ → *NH₂NH + *NH₃ ($\Delta G = -0.80$ eV), *NH₂NH → *NH₂ + *NH₃ ($\Delta G = 0.05$ eV). In addition, the hydrogenation of *NH₂NH₂ was a key process in NRR, in which *NH₂NH₂ was rapidly hydrogenated to *NH₂

and *NH₃. The synergistic effect of Fe/Ti dual active sites on *NH₂NH intermediates promoted the conversion of *NH₂NH₂ to *NH₂ + *NH₃ [48]. Finally, the energy consumed for the desorption of NH₃ during the whole NRR process was 1.24 eV. More importantly, the adsorption and hydrogenation of N₂ to generate *NNH ($\Delta G = 1.43$ eV) was a rate control step in the entire N₂ immobilization process. In summary, the above calculations indicated that the synergistic effect of Fe and Ti introduced in TiO₂ (101) promoted the adsorption of nitrogen and further promoted the N₂ activation. Currently, the enhancement of NRR activity was mainly due to the synergistic effect of OV with dual Fe/Ti active sites [49–51].

4. Conclusion

In summary, Fe-doped TiO₂ with MIL-125(Ti) as a precursor prepared by a novel FJH method was an effective catalyst for photocatalytic nitrogen fixation. FJH treatment produced lattice defects that promoted the nitrogen reduction ability. The experimental results indicated that the Fe/TiO₂ photocatalyst formed under FJH exhibited a strong binding interaction between the doped Fe and MOF materials and its ammonia production rate reached 56.87 μmol g⁻¹ h⁻¹ without adding any sacrificial agent and co-catalyst, which was 4.3 times higher than pristine TiO₂. DFT calculations further verified the synergistic effect between the lattice defects, OV and the Fe/Ti dual active sites which made the improvement in NRR activity. This work provided a new method (FJH method) to prepare a highly-efficient photocatalyst for artificial nitrogen fixation.

CRediT authorship contribution statement

Yang Huiying: Investigation, Writing – original draft. **Li Zizhen:** Investigation, Writing – review & editing. **Ren Guangmin:** Investigation. **Meng Xiangchao:** Investigation, Supervision, Writing – review & editing. **Zhang Zisheng:** Investigation, Writing – review & editing.

Declaration of Competing Interest

The authors declare that they have no known competing financial interests or personal relationships that could have appeared to influence the work reported in this paper.

Data Availability

Data will be made available on request.

Acknowledgment

This work was financially supported by the National Natural Science Foundation of China (Grant No: 22002146), Shandong Provincial Natural Science Foundation (Grant No.: ZR2021QB056), the Fundamental Research Funds for the Central Universities (No.: 202261014), and Taishan Scholars Foundation of Shandong Province (No.: tsqn201909058). The authors would like to thank Shiyanjia Lab (<https://www.shiyanjia.com>) for the XPS, SEM, FTIR, etc. analysis. The authors would like to thank eceshi Lab (<https://www.eceshi.com>) for the EPR, In-suit XPS, TPD, PL, etc. analysis.

Appendix A. Supporting information

Supplementary data associated with this article can be found in the online version at [doi:10.1016/j.apcatb.2024.123795](https://doi.org/10.1016/j.apcatb.2024.123795).

References

- [1] F. Rizzioli, D. Bertasini, D. Bolzonella, N. Frison, F.J.S. Battista, F. Technology, A critical review on the techno-economic feasibility of nutrients recovery from anaerobic digestate in the agricultural sector, *Sep. Purif. Technol.* 306 (2022) 122690, <https://doi.org/10.1016/j.seppur.2022.122690>.
- [2] A.I. Osman, N. Mehta, A.M. Elgarayh, M. Hefny, A. Al-Hinai, Hydrogen production, storage, utilisation and environmental impacts: a review, *Environ. Chem. Lett.* 20 (2022) 2213, <https://doi.org/10.1007/s10311-022-01432-x>.
- [3] S. Kanwal, M.T. Mehran, M. Hassan, M. Anwar, S.R. Naqvi, A.H. Khoja, An integrated future approach for the energy security of Pakistan: Replacement of fossil fuels with syngas for better environment and socio-economic development, *Renew. Sust. Energ. Rev.* 156 (2022) 111978, <https://doi.org/10.1016/j.rser.2021.111978>.
- [4] T. Xu, J. Liang, S. Li, Z. Xu, L. Yue, T. Li, Y. Luo, Q. Liu, X. Shi, A.M. Asiri, Recent advances in nonprecious metal oxide electrocatalysts and photocatalysts for N₂ reduction reaction under ambient condition, *Small Sci.* 1 (2021) 2000069, <https://doi.org/10.1002/smss.202000069>.
- [5] R. Shi, X. Zhang, G.I. Waterhouse, Y. Zhao, T. Zhang, The journey toward low temperature, low pressure catalytic nitrogen fixation, *Adv. Energy Mater.* 10 (2020) 2000659, <https://doi.org/10.1002/aenm.202000659>.
- [6] S. Padinjarekutt, H. Li, S. Ren, P. Ramesh, F. Zhou, S. Li, G. Belfort, M. Yu, Na plus-gated nanochannel membrane for highly selective ammonia (NH₃) separation in the Haber-Bosch process, *Chem. Eng. J.* 454 (2023) 139998, <https://doi.org/10.1016/j.cej.2022.139998>.
- [7] B. Lin, F.H. Nowrin, J.J. Rosenthal, A.S. Bhowan, M. Malmali, Perspective on intensification of haber-bosch to enable ammonia production under milder conditions, *ACS Sustain. Chem. Eng.* 11 (2023) 9880–9899, <https://doi.org/10.1021/acssuschemeng.2c06711>.
- [8] H. Liu, M. Cheng, Y. Liu, J. Wang, G. Zhang, L. Li, L. Du, G. Wang, S. Yang, X. Wang, Single atoms meet metal-organic frameworks: collaborative efforts for efficient photocatalysis, *Energy Environ. Sci.* 15 (2022) 3722–3749, <https://doi.org/10.1039/d2ee01037b>.
- [9] D. Gao, J. Xu, L. Wang, B. Zhu, H. Yu, J. Yu, Optimizing atomic hydrogen desorption of sulfur-rich NiS_{1+x} cocatalyst for boosting photocatalytic H₂ evolution, *Adv. Mater.* 34 (2022) 2108475, <https://doi.org/10.1002/adma.202108475>.
- [10] C. Yang, Y. Zhang, F. Yue, R. Du, T. Ma, Y. Bian, R. Li, L. Guo, D. Wang, F. Fu, Co doping regulating electronic structure of Bi₂MoO₆ to construct dual active sites for photocatalytic nitrogen fixation, *Appl. Catal. B* 338 (2023) 123057, <https://doi.org/10.1016/j.apcatb.2023.123057>.
- [11] S.J. Forrest, B. Schlusshass, E.Y. Yuzik-Klimova, S. Schneider, Nitrogen fixation via splitting into nitrido complexes, *Chem. Rev.* 121 (2021) 6522–6587, <https://doi.org/10.1021/acs.chemrev.0c00958>.
- [12] C. Zhao, Z. Wang, X. Chen, H. Chu, H. Fu, C. Wang, Robust photocatalytic benzene degradation using mesoporous disk-like N-TiO₂ derived from MIL-125 (Ti), *Chin. J. Catal.* 41 (2020) 1186–1197, [https://doi.org/10.1016/S1872-2067\(19\)63516-3](https://doi.org/10.1016/S1872-2067(19)63516-3).
- [13] J. Chen, X. Zhang, F. Bi, X. Zhang, Y. Yang, Y. Wang, A facile synthesis for uniform tablet-like TiO₂/C derived from Materials of Institut Lavoisier-125 (Ti)(MIL-125 (Ti)) and their enhanced visible light-driven photodegradation of tetracycline, *J. Colloid Interface Sci.* 571 (2020) 275–284, <https://doi.org/10.1016/j.jcis.2020.03.055>.
- [14] S. Zhang, X. Yi, G. Hu, M. Chen, H. Shen, B. Li, L. Yang, W. Dai, J. Zou, S. Luo, Configuration regulation of active sites by accurate doping inducing self-adapting defect for enhanced photocatalytic applications: a review, *Coord. Chem. Rev.* 478 (2023) 214970, <https://doi.org/10.1016/j.ccr.2022.214970>.
- [15] Y. Ren, Y. Han, Z. Li, X. Liu, S. Zhu, Y. Liang, K. Yeung, S. Wu, Ce and Er Co-doped TiO₂ for rapid bacteria-killing using visible light, *Bioact. Mater.* 5 (2020) 201–209, <https://doi.org/10.1016/j.bioactmat.2020.02.005>.
- [16] B. Lei, W. Cui, J. Sheng, H. Wang, P. Chen, J. Li, Y. Sun, F. Dong, Synergistic effects of crystal structure and oxygen vacancy on Bi₂O₃ polymorphs: intermediates activation, photocatalytic reaction efficiency, and conversion pathway, *Sci. Bull.* 65 (2020) 467–476, <https://doi.org/10.1016/j.scib.2020.01.007>.
- [17] Y. Bo, H. Wang, Y. Lin, T. Yang, R. Ye, Y. Li, C. Hu, P. Du, Y. Hu, Z. Liu, Altering hydrogenation pathways in photocatalytic nitrogen fixation by tuning local electronic structure of oxygen vacancy with dopant, *Angew. Chem. Int. Ed.* 60 (2021) 16085–16092, <https://doi.org/10.1002/anie.202104001>.
- [18] S. Wu, Z. Chen, W. Yue, S. Mine, T. Toyao, M. Matsuoka, X. Xi, L. Wang, J. Zhang, Single-atom high-valent Fe (IV) for promoted photocatalytic nitrogen hydrogenation on porous TiO₂-SiO₂, *ACS Catal.* 11 (2021) 4362–4371, <https://doi.org/10.1021/acscatal.1c00072>.
- [19] T. Wu, X. Zhu, Z. Xing, S. Mou, C. Li, Y. Qiao, Q. Liu, Y. Luo, X. Shi, Y. Zhang, Greatly improving electrochemical N₂ reduction over TiO₂ nanoparticles by iron doping, *Angew. Chem. Int. Ed.* 58 (2019) 18449–18453, <https://doi.org/10.1002/anie.201911153>.
- [20] M. Valero-Romero, J. Santaclara, L. Oar-Arteta, L. Van Koppen, D. Osadchii, J. Gascon, F. Kapteijn, Photocatalytic properties of TiO₂ and Fe-doped TiO₂ prepared by metal organic framework-mediated synthesis, *Chem. Eng. J.* 360 (2019) 75–88, <https://doi.org/10.1016/j.cej.2018.11.132>.
- [21] Z. Zhao, J. Sun, X. Li, Z. Zhang, X. Meng, Joule heating synthesis of NiFe alloy/MoO₂ and in-situ transformed (Ni,Fe)OOH/MoO₂ heterostructure as effective complementary electrocatalysts for overall splitting in alkaline seawater, *Appl. Catal. B* 340 (2024) 123277, <https://doi.org/10.1016/j.apcatb.2023.123277>.
- [22] Z. Zhao, G. Ren, Z. Zhang, X. Meng, Z. Li, Rapid Joule heating synthesis of Pt clusters on C₃N₄ with abundant nitrogen vacancies for highly-efficiently photocatalytic H₂ production, *Sep. Purif. Technol.* 330 (2023) 125393, <https://doi.org/10.1016/j.seppur.2023.125393>.
- [23] G. Ren, Z. Zhao, Z. Li, Z. Zhang, X. Meng, Rapid Joule-Heating fabrication of oxygen vacancies and anchor of Ru clusters onto BiVO₄ for greatly enhanced Photocatalytic N₂ Fixation, *J. Catal.* 428 (2023) 115147, <https://doi.org/10.1016/j.jcat.2023.115147>.
- [24] J. Sun, S. Qin, Z. Zhang, C. Li, X. Xu, Z. Li, X. Meng, Joule heating synthesis of well lattice-matched Co₂Mo₃O₈/MoO₂ heterointerfaces with greatly improved hydrogen evolution reaction in alkaline seawater electrolysis with 12.4% STH efficiency, *Appl. Catal. B* 338 (2023) 123015, <https://doi.org/10.1016/j.apcatb.2023.123015>.
- [25] J. Ma, W. Liu, X. Liang, B. Quan, Y. Cheng, G. Ji, W. Meng, Nanoporous TiO₂/C composites synthesized from directly pyrolysis of a Ti-based MOFs MIL-125 (Ti) for efficient microwave absorption, *J. Alloy. Compd.* 728 (2017) 138–144, <https://doi.org/10.1016/j.jallcom.2017.08.274>.
- [26] A.A. Ismail, D.W. Bahnemann, One-step synthesis of mesoporous platinum/titania nanocomposites as photocatalyst with enhanced photocatalytic activity for methanol oxidation, *Green. Chem.* 13 (2011) 428–435, <https://doi.org/10.1039/c0gc00744g>.
- [27] K. Gao, J. Chen, Z. Liu, Y. Li, Y. Wu, J. Zhao, P. Na, Intensified redox co-conversion of As (III) and Cr (VI) with MIL-125 (Ti)-derived COOH functionalized TiO₂: Performance and mechanism, *Chem. Eng. J.* 360 (2019) 1223–1232, <https://doi.org/10.1016/j.cej.2018.09.134>.
- [28] H. Wang, N. Zhang, G. Cheng, H. Guo, Z. Shen, L. Yang, Y. Zhao, A. Alsaedi, T. Hayat, X. Wang, Preparing a photocatalytic Fe doped TiO₂/rGO for enhanced bisphenol A and its analogues degradation in water sample, *Appl. Surf. Sci.* 505 (2020) 144640, <https://doi.org/10.1016/j.apsusc.2019.144640>.
- [29] S. Saraiva, P. Pereira, C. Paula, R. Rebelo, J.F. Coelho, A.C. Serra, A. Fonseca, Development of electrospun mats based on hydrophobic hydroxypropyl cellulose derivatives, *Mater. Sci. Eng. C* 131 (2021) 112498, <https://doi.org/10.1016/j.msec.2021.112498>.
- [30] Y. Wan, H. Jiang, Y. Ren, Y. Liu, L. Zhang, Q. Lei, D. Zhu, J. Liu, X. Zhang, N. Ma, Photothermal self-healable polypyrrole-polyurethane sponge with dynamic covalent oximino bonds for flexible strain sensors, *Eur. Polym. J.* 193 (2023) 112097, <https://doi.org/10.1016/j.eurpolymj.2023.112097>.
- [31] M.Z. Hussain, M. Bahri, W.R. Heinz, Q. Jia, O. Ersen, T. Kratky, R.A. Fischer, Y. Zhu, Y. Xia, An in situ investigation of the thermal decomposition of metal-organic framework NH₂-MIL-125 (Ti), *Microporous Mesoporous Mater.* 316 (2021) 110957, <https://doi.org/10.1016/j.micromeso.2021.110957>.
- [32] M. Gronli, M.J. Antal, G. Várhegyi, A round-robin study of cellulose pyrolysis kinetics by thermogravimetry, *Ind. Eng. Chem. Res.* 38 (1999) 2238–2244, <https://doi.org/10.1021/ie980601n>.

- [33] A. Mancuso, N. Morante, M. De Carluccio, O. Sacco, L. Rizzo, M. Fontana, S. Esposito, V. Vaiano, D. Sannino, Solar driven photocatalysis using iron and chromium doped TiO₂ coupled to moving bed biofilm process for olive mill wastewater treatment, *Chem. Eng. J.* 450 (2022) 138107, <https://doi.org/10.1016/j.cej.2022.138107>.
- [34] Y. Wang, Y. Tian, J. Zhang, C. Yu, R. Cai, J. Wang, Y. Zhang, J. Wu, Y. Wu, Tuning morphology and electronic structure of amorphous NiFeB nanosheets for enhanced electrocatalytic N₂ reduction, *ACS Appl. Energy Mater.* 3 (2020) 9516–9522, <https://doi.org/10.1021/acs.aem.0c01834>.
- [35] M. Zhang, G. Li, Q. Li, J. Chen, E.A. Elimian, H. Jia, H. He, In situ construction of manganese oxide photothermocatalysts for the deep removal of toluene by highly utilizing sunlight energy, *Environ. Sci. Technol.* 57 (2023) 4286–4297, <https://doi.org/10.1021/acs.est.2c09136>.
- [36] S. Ghasemi, S. Rahimnejad, S.R. Setayesh, S. Rohani, M. Gholami, Transition metal ions effect on the properties and photocatalytic activity of nanocrystalline TiO₂ prepared in an ionic liquid, *J. Hazard. Mater.* 172 (2009) 1573–1578, <https://doi.org/10.1016/j.jhazmat.2009.08.029>.
- [37] M. Zanjanchi, H. Noei, M. Moghimi, Rapid determination of aluminum by UV–vis diffuse reflectance spectroscopy with application of suitable adsorbents, *Talanta* 70 (2006) 933–939, <https://doi.org/10.1016/j.talanta.2006.05.056>.
- [38] G. Ren, M. Shi, Z. Li, Z. Zhang, X. Meng, Electronic metal-support interaction via defective-induced platinum modified BiOBr for photocatalytic N₂ fixation, *Appl. Catal. B* 327 (2023) 122462, <https://doi.org/10.1016/j.apcatb.2023.122462>.
- [39] Z. Wang, Y. Huang, W. Ho, J. Cao, Z. Shen, S.C. Lee, Fabrication of Bi₂O₂CO₃/g-C₃N₄ heterojunctions for efficiently photocatalytic NO in air removal: In-situ self-sacrificial synthesis, characterizations and mechanistic study, *Appl. Catal. B* 199 (2016) 123–133, <https://doi.org/10.1016/j.apcatb.2016.06.027>.
- [40] Z. Jin, Y. Wu, Novel preparation strategy of graphdiyne (CnH_{2n-2}): One-pot conjugation and S-Scheme heterojunctions formed with MoP characterized with in situ XPS for efficiently photocatalytic hydrogen evolution, *Appl. Catal. B* 327 (2023) 122461, <https://doi.org/10.1016/j.apcatb.2023.122461>.
- [41] J. Wang, D.N. Tafen, J.P. Lewis, Z. Hong, A. Manivannan, M. Zhi, M. Li, N. Wu, Origin of photocatalytic activity of nitrogen-doped TiO₂ nanobelts, *J. Am. Chem. Soc.* 131 (2009) 12290–12297, <https://doi.org/10.1021/ja903781h>.
- [42] G. Yang, T. Wang, B. Yang, Z. Yan, S. Ding, T. Xiao, Enhanced visible-light activity of F-N co-doped TiO₂ nanocrystals via nonmetal impurity, Ti³⁺ ions and oxygen vacancies, *Appl. Surf. Sci.* 287 (2013) 135–142, <https://doi.org/10.1016/j.apsusc.2013.09.094>.
- [43] P. Li, Z. Zhou, Q. Wang, M. Guo, S. Chen, J. Low, R. Long, W. Liu, P. Ding, Y. Wu, Y. Xiong, Visible-light-driven nitrogen fixation catalyzed by Bi₅O₇Br nanostructures: enhanced performance by oxygen vacancies, *J. Am. Chem. Soc.* 142 (2020) 12430–12439, <https://doi.org/10.1021/jacs.0c05097>.
- [44] Y. Zhang, L. Ran, Y. Zhang, P. Zhai, Y. Wu, J. Gao, Z. Li, B. Zhang, C. Wang, Z. Fan, X. Zhang, J. Cao, D. Jin, L. Sun, J. Hou, Two-dimensional defective boron-doped niobic acid nanosheets for robust nitrogen photofixation, *ACS Nano* 15 (2021) 17820–17830, <https://doi.org/10.1021/acs.nano.1c06017>.
- [45] Z. Zhang, N. Lu, W. Cai, J. Wen, K. Li, H. Qu, A novel Zn-doped CHA zeolite coupled CDs for photocatalytic nitrogen fixation, *Mol. Catal.* 549 (2023) 113471, <https://doi.org/10.1016/j.mcat.2023.113471>.
- [46] Z. Guo, T. Wang, H. Liu, S. Qiu, X. Zhang, Y. Xu, S.J. Langford, C. Sun, Defective 2D silicon phosphide monolayers for the nitrogen reduction reaction: a DFT study, *Nanoscale* 14 (2022) 5782–5793, <https://doi.org/10.1039/d1nr08445c>.
- [47] G. Ren, M. Shi, S. Liu, Z. Li, Z. Zhang, X. Meng, Molecular-level insight into photocatalytic reduction of N₂ over Ruthenium single atom modified TiO₂ by electronic Metal-support interaction, *Chem. Eng. J.* 454 (2023), <https://doi.org/10.1016/j.cej.2022.140158>.
- [48] W. Zhang, G. Pan, D. Han, T. Liu, W. Liang, M. Dai, H. Xie, D. Qin, L. Niu, Regulating bimetallic active centers for exploring the structure-activity relationship toward high-performance photocatalytic nitrogen reduction, *Mater. Today* 22 (2023) 100323, <https://doi.org/10.1016/j.mtnano.2023.100323>.
- [49] M. Chen, D. Liu, L. Qiao, P. Zhou, J. Feng, K.W. Ng, Q. Liu, S. Wang, H. Pan, In-situ/operando Raman techniques for in-depth understanding on electrocatalysis, *Chem. Eng. J.* 461 (2023) 141939, <https://doi.org/10.1016/j.cej.2023.141939>.
- [50] Z. Qian, R. Zhang, Y. Xiao, H. Huang, Y. Sun, Y. Chen, T. Ma, X. Sun, Trace to the source: self-tuning of MOF photocatalysts, *Adv. Energy Mater.* 13 (2023) 2300086, <https://doi.org/10.1002/aenm.202300086>.
- [51] G. Ren, J. Zhao, Z. Zhao, Z. Li, L. Wang, Z. Zhang, C. Li, X. Meng, Defects-induced single-atom anchoring on metal–organic frameworks for high-efficiency photocatalytic nitrogen reduction, *Angew. Chem. Int. Ed.* 63 (2023) e202314408, <https://doi.org/10.1002/anie.202314408>.